Advanced Energy Materials

ADVANCED ENERGY MATERIALS
www.advenergymat.de

RESEARCH ARTICLE

Recyclable Triboelectric Nanogenerators Enabled by Biodegradable Pollen-Paper Nanoarchitectonics for Sustainable Energy Harvesting

Chenchen Zhou[1,2,3] | Zihao Guo[4] | Jun Hao Mo[2,3] | Licong Yang[2,3] | Hailu Wang[2,3] | Daru Seto Bagus Anugrah[2,3] | Munho Kim[4] | Dan Sun[5] | Nam-Joon Cho[2,3]

[1]State Key Laboratory of Micro-nano Engineering Science, School of Mechanical Engineering, Shanghai Jiao Tong University, Shanghai, China | [2]School of Materials Science and Engineering, Nanyang Technological University, Singapore, Singapore | [3]Centre for Cross Economy, Nanyang Technological University, Singapore, Singapore | [4]School of Electrical and Electronic Engineering, Nanyang Technological University, Singapore, Singapore | [5]School of Material Science & Chemical Engineering, Hubei University of Technology, Wuhan, China

Correspondence: Munho Kim (munho.kim@ntu.edu.sg) | Dan Sun (sundan0806@mail.hbut.edu.cn) | Nam-Joon Cho (njcho@ntu.edu.sg)

Received: 7 June 2026 | **Revised:** 11 August 2026 | **Accepted:** 20 August 2026

Keywords: bleaching modification | pollen paper | self-powered wearable systems | sustainable energy harvesting | triboelectric nanogenerators (TENGs)

ABSTRACT

Triboelectric nanogenerators (TENGs) are promising devices for harvesting ambient mechanical energy, however, their development is hindered by low power output, limited energy conversion efficiency, and reliance on synthetic polymers. Here, we report a pollen-based recyclable TENG (PRTENG) achieving a power density of 5.07 W m^{-2}, rivaling synthetic polymeric TENGs. The seamless integration of bleached pollen paper with PEDOT:PSS and poly(vinyl alcohol) via strong hydrogen-bonding networks exhibits a 21% increase in maximum stress and 82-fold toughness enhancement alongside robust durability of over 100 000 contact-separation cycles. Moreover, when integrated into footwear, the PRTENG effectively converts human motion into electrical energy. Critically, water-assisted disassembly enables complete component recovery for reassembly with negligible performance loss, while the recovered substrates can biodegrade within 12 days. Overall, this study provides a sustainable approach to engineer fully flexible, recyclable, and eco-friendly TENGs for deployment in wearable electronics, decentralized sensing networks, and next-generation sustainable IoT infrastructures.

1 | Introduction

With the rapid proliferation of the Internet of Things (IoT), wearable electronics, and intelligent sensing systems, the demand for sustainable and portable power sources has surged dramatically (Figure 1A) [1–3]. Conventional energy storage devices, such as lithium-ion batteries, dominate the current market due to their high energy density; however, their intrinsic limitations—including finite cycle life, prohibitive replacement costs, and severe environmental burdens arising from toxic and hazardous components and non-recyclable packaging-–pose formidable challenges to long-term sustainability [4–7]. In this context, triboelectric nanogenerators (TENGs) have emerged as a promising alternative energy harvesting technology [8–10], garnering extensive research attention due to their ability to efficiently convert ubiquitous mechanical energy from human motion (e.g., walking or finger tapping) [11, 12], machine vibrations [13, 14], and ambient stimuli (e.g., wind or water flow) [15–17] into

Chenchen Zhou and Zihao Guo contributed equally to this work.

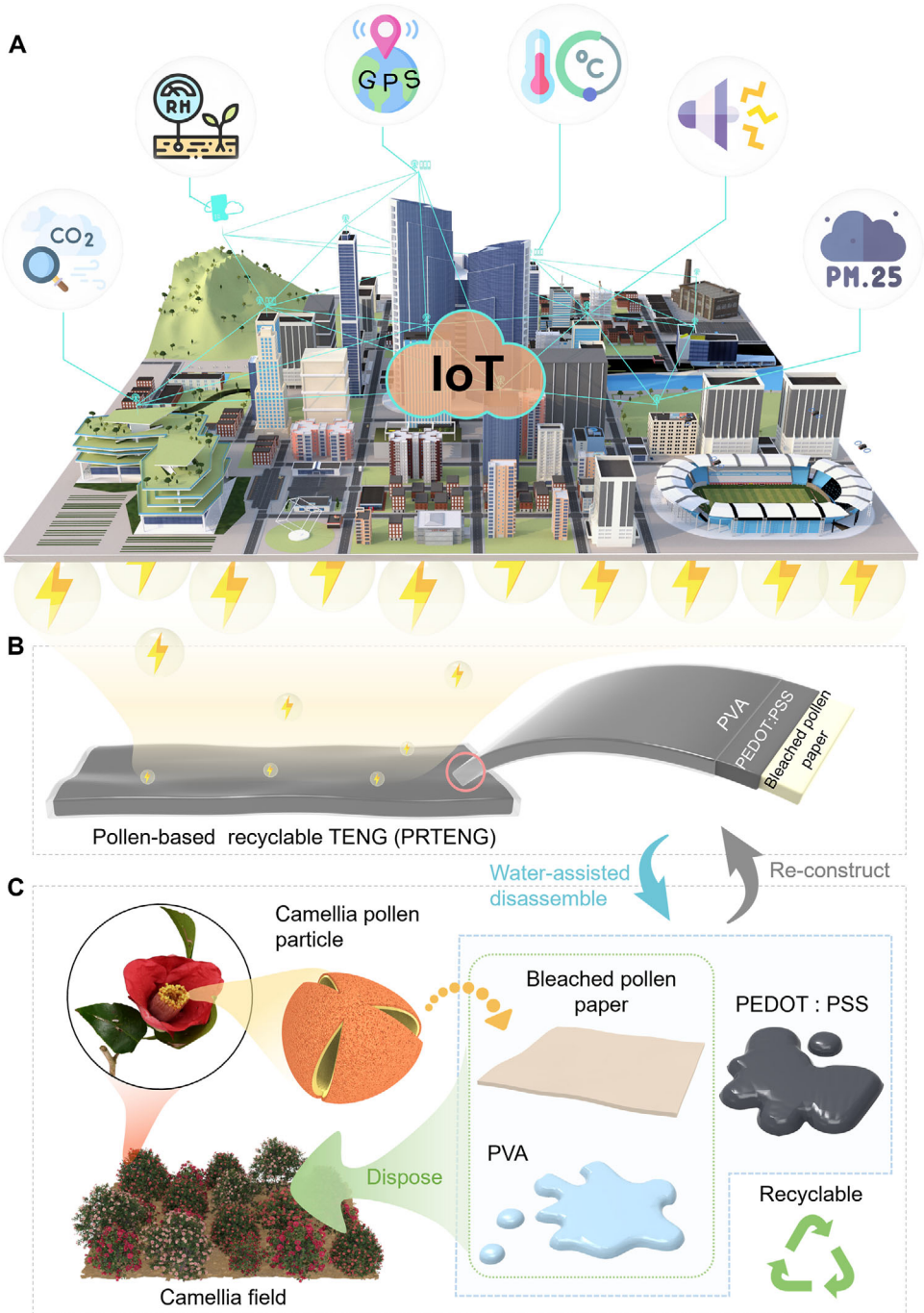

FIGURE 1 | Pollen-based recyclable triboelectric nanogenerator (PRTENG) for sustainable power and circular use. (A) Conceptual illustration of distributed, self-powered IoT nodes for environmental monitoring (relative humidity, GPS, temperature, CO_2, noise, and $PM_{2.5}$). (B) Device architecture of the PRTENG, comprising poly(vinyl alcohol) (PVA) as the triboelectric layer, PEDOT:PSS as the conducting electrode, and bleached pollen paper as the supporting layer, enabling device re-construction. (C) Closed-loop end-of-life pathway enabled by biomass sourcing (camellia pollen) and water-assisted disassembly to separate bleached pollen paper, PVA, and PEDOT:PSS for disposal and/or recycling.

electricity via the coupled effects of triboelectrification and electrostatic induction [18–21]. Endowed with inherent advantages of lightweight construction, structural flexibility, and material versatility [22–24]—encompassing synthetic polymers, functional textiles, and biodegradable composites [25–31]—TENGs have been widely exploited in self-powered sensing scenarios, ranging from health monitoring patches and environmental sensors to human-machine interfaces [8, 32, 33].

Despite these compelling merits, the scalable adoption of TENGs is mainly hindered by two interrelated challenges. First, most high-performance TENGs rely on non-biodegradable fossil-derived polymers (e.g., PE, PET, polydimethylsiloxane (PDMS)) and metallic electrodes, whose production and end-of-life disposal generate persistent electronic waste, microplastic pollution, and toxic leaching, directly conflicting with green energy principles and global carbon-neutrality goals [34–38]. Second, while

renewable and biodegradable materials (e.g., cellulose, chitosan, gelatin) have been explored to mitigate environmental impacts [34, 39, 40], they typically suffer from unsatisfactory power output and low energy-conversion efficiency. For instance, bacterial nanocellulose- and lignocellulose-based TENGs deliver peak power densities of only 4.8 and 27.2 mW m^{-2} [41, 42], and even modified cellulose systems rarely exceed 2.6 W m^{-2} [43]. This stark performance gap underscores an urgent, unmet need: the development of high-performance TENGs that simultaneously achieve full-life-cycle sustainability and competitive electrical output, thereby reconciling the long-standing trade-off between eco-friendliness and electrical performance.

Among emerging sustainable materials, pollen–-an abundant, renewable biomass sourced from flowering plants and often described as the "diamond of the organic world" for its distinctive microstructures and properties [44]–-exhibits tremendous potential for fabricating eco-friendly substrates, thereby addressing the sustainability predicament of TENGs. Typically, raw pollen is subjected to sequential defatting and alkali treatment to eliminate surface lipid impurities and loosen its rigid exine structure, thereby enabling the formation of flexible, porous, and mechanically robust pollen paper via subsequent molding and drying processes [45, 46]. Benefiting from its intrinsic biodegradability, biocompatibility, and structural tunability, pollen paper has been successfully employed as a green substrate for various electronic devices, including solar cells, pressure sensors, and flexible electronics in previous studies, with recent advances highlighting biomass-derived papers as promising candidates for green electronic platforms [47]. However, the direct application of pollen paper in TENG is further constrained by its suboptimal hydrophilicity and intrinsic structural toughness. These inherent characteristics lead to poor interfacial conformability with device substrate during TENG fabrication, which severely compromises contact stability and ultimately degrades the triboelectric performance of TENGs–-a critical limitation that is also prevalent in other biomass-based TENG substrates, where precise surface property modulation is indispensable for optimizing triboelectric response [48]. To mitigate these issues, this study integrates a targeted bleaching treatment into the pollen paper preparation process. This bleaching step not only efficiently removes residual impurities that are recalcitrant to conventional defatting and alkali treatment but also modifies the surface chemical properties of pollen paper, endowing it with lightweight features, enhanced substrate affinity, and improved surface uniformity (Figure 1B). These synergistic modifications collectively optimize the triboelectric activity of pollen paper, rendering it an ideal substrate for high-performance TENGs. Despite the significant progress in pollen paper-based functional electronics, its application in energy harvesting–-particularly for TENGs with tailored modification to enhance mechanical-to-electrical energy conversion–-remains largely underexplored, creating a notable research gap in the field of sustainable energy harvesters.

To bridge this research gap and tackle the aforementioned challenges, we report a high-output, flexible, fully recyclable, and eco-friendly TENG based on bleached pollen paper (Figure 1C). In this design, the biomass-derived pollen paper (modified via the proposed bleaching strategy) eliminates the reliance on petroleum-based polymers, ensuring inherent environmental compatibility. Paired with poly(3,4-ethylenedioxythiophene):polystyrenesulfonate (PEDOT:PSS) as a conducting electrode, the fabricated pollen-based recyclable TENG (PRTENG) delivers a remarkable peak power density of 5.07 W m^{-2}–-comparable to that of state-of-the-art synthetic polymer-based TENGs–-while maintaining robust mechanical durability over 30 000 cycles through controlled microstructuring and contact interface optimization. Furthermore, the utilization of low-cost and recyclable pollen paper facilitates scalable device fabrication and promotes closed-loop material cycles, with the bleaching modification serving as a key innovation to enhance triboelectric performance. As a proof of concept, a practical wearable self-powered system is demonstrated by integrating the PRTENG into footwear, which can effectively charge an electronic watch during routine walking. Overall, this work not only develops an innovative, high-performance eco-friendly TENG but also establishes a scalable material paradigm that aligns with global carbon-neutrality and cross-economy goals [49], paving the way for the next generation of sustainable energy harvesting devices.

2 | Results and Discussion

2.1 | Bleaching-Induced Chemical, Structural, Mechanical Evolution of Pollen Paper

The original Camellia pollen paper (OP) is fabricated by casting the defatted and alkali-treated Camellia pollen microparticle suspension followed by air drying [44], yielding a mechanically robust but optically semitransparent film with a characteristic orange color (Figure 2A). Subsequent NaClO bleaching removes the chromophores, producing a visually uniform white pollen paper (BP), indicative of substantial chemical modification. At the molecular level, sporopollenin–-the primary constituent of OP–-contains hydroxyl, carboxyl, and aromatic moieties arising from partial de-esterification during alkaline treatment [50]. These aromatic domains give rise to the pronounced absorption band at 1576 cm^{-1} in the FTIR spectrum (Figure 2B), corresponding to aromatic C═C skeletal vibrations and underpinning the visible-light absorption responsible for the native coloration. Bleaching induces a marked attenuation of these aromatic features, accompanied by the emergence of a strong carbonyl stretching band at 1706 cm^{-1} and a new XPS C 1s component at 289 eV (Figure 2B,C), characteristic of highly oxidized carbon species. These changes signify oxidative cleavage of conjugated aromatic domains into largely non-conjugated oxygenated functionalities, including carboxyls and ketones. As a result, the effective π-conjugation length is substantially reduced, suppressing $\pi \rightarrow \pi^*$ electronic transitions in the visible region. Importantly, the persistence of C—O and C—O—C vibrational bands (1185–1011 cm^{-1}) confirms that the backbone sporopollenin framework remains largely intact, despite extensive modification of its chromophoric components.

Beyond chemical transformation, bleaching profoundly alters the hierarchical structure of the pollen paper. Prior to bleaching, OP is composed of densely stacked, flattened pollen-derived building blocks, exhibiting a thickness of 50.6 ± 1.0 μm and a surface roughness of 0.633 ± 0.055 μm (Figure 2D and S1). Oxidative treatment partially removes constituent components

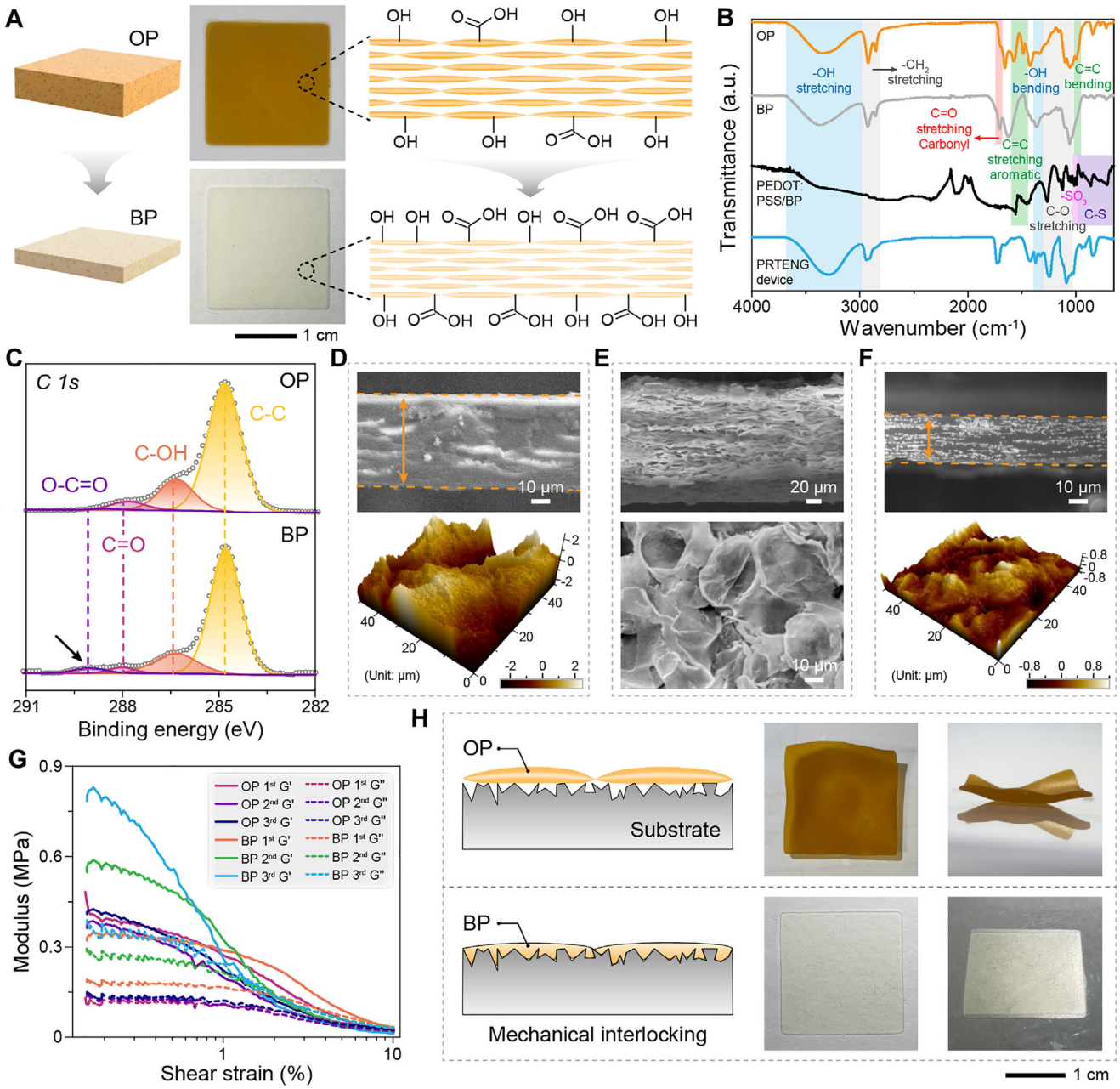

FIGURE 2 | Chemical, structural, and mechanical evolution of Camellia pollen paper induced by bleaching. (A) Optical images and schematic illustrations comparing the morphology and chemical functionality of original pollen paper (OP) and bleached pollen paper (BP), highlighting the removal of chromophoric components and the introduction of oxygen-containing functional groups after bleaching. (B) FTIR spectra of OP, BP, PEDOT:PSS-coated BP (PEDOT:PSS/BP), and the complete PRTENG device, showing attenuation of aromatic C═C vibrations and the emergence of carbonyl-related absorptions upon bleaching. (C) High-resolution XPS C 1s spectra of OP and BP, revealing the emergence of a peak for O—C═O after NaClO treatment. (D) Cross-sectional SEM image and surface AFM topography of OP, showing a dense laminated structure with relatively high surface roughness. (E) Cross-sectional and surface SEM images of freeze-dried BP, exhibiting a highly porous architecture. (F) Cross-sectional SEM image and surface AFM topography of ambient-dried BP, demonstrating pronounced thickness shrinkage, structural densification, and reduced surface roughness. (G) Strain-dependent viscoelastic moduli of OP and BP, showing the storage modulus (G') and loss modulus (G'') under repeated shear loading. (H) Schematic illustrations and corresponding optical images comparing the weak substrate adhesion of OP with the strong mechanical interlocking and conformal adhesion of BP on a rigid substrate after drying.

and introduces a highly hydrophilic, polysaccharide-rich network that readily swells in water. After ethanol exchange and freeze-drying, BP expands dramatically to 136.7 ± 8.1 μm, approximately 2.7 times thicker than OP, and exhibits a markedly loosened architecture characterized by a highly porous internal network as well as a roughened surface (Figure 2E). In contrast, drying BP under ambient conditions leads to pronounced thickness shrinkage to 25.0 ± 0.9 μm (Figure 2F), accompanied by a transition from opaque white to optically transparent (Figure S2). This behavior originates from capillary forces generated

during solvent evaporation. In the hydrated state, water occupies the interconnected micro- and nanopores, preserving structural separation within the fibrous network. As evaporation proceeds, air–water interfaces form and generate capillary pressures that exceed the elastic restoring forces of the softened framework, driving irreversible densification and pore collapse. The resulting reduction in surface roughness to 0.270 ± 0.018 μm and the elimination of sub-wavelength scattering centers significantly suppress light scattering. Combined with the removal of chromophoric species during bleaching, these structural changes enable high optical transparency in the dried BP.

The chemical and morphological evolution of BP is further reflected in its dynamic mechanical response. Amplitude-sweep rheological measurements performed under a constant normal force of 1 N reveal solid-like viscoelastic behavior for both OP and BP at low shear strain, with storage moduli (G') consistently exceeding loss moduli (G''), indicative of percolated fibrous networks capable of storing elastic energy (Figure 2G). As strain increases, both moduli decrease, signaling progressive network disruption. Notably, OP shows minimal variation in G' and G'' across repeated measurements, suggesting a relatively compliant and partially recoverable microstructure. In stark contrast, BP exhibits pronounced loading-history dependence: the low-strain G' and G'' increase substantially from the first to the third measurement. This progressive stiffening indicates irreversible, stress-induced densification and mechanical reinforcement of the bleached network, driven by enhanced inter-fiber contacts and hydrogen bonding between exposed surfaces rich in oxygen-containing functional groups. Besides, bleaching removes compliant or energy-dissipating constituents, resulting in a lower G' and a higher G'' for BP compared with OP at their pristine stage, indicating a more viscous-dominated, highly deformable network with enhanced conformability. The higher stiffness of OP limits wetting and suppresses interlocking, resulting in weak adhesion. In contrast, BP can more readily undergo shape adaptation during drying, enabling tight adhesion to the underlying substrate and effective embedding and mechanical interlocking within the micro/nanoscale asperities of the substrate surface under capillary forces (Figure 2H). As a result, BP can be firmly fixed onto substrates without warping or delamination, providing a mechanically stable and process-friendly platform for subsequent device integration.

2.2 | Interfacial Integration and Mechanical Reinforcement in Flexible PRTENGs

An aqueous suspension of poly(3,4-ethylenedioxythiophene): poly(styrene sulfonate) (PEDOT:PSS) was employed to construct the conductive electrode of the PRTENG. Owing to its hygroscopic and swelling nature, pollen paper exhibits a pronounced response to moisture exposure [45]. When OP approaches a pendant PEDOT:PSS droplet, the localized humidity induces out-of-plane deformation even prior to direct contact. Upon droplet deposition, water uptake at the contact region leads to progressive swelling and ultimately results in a pronounced bulge morphology (Figure 3A(i) and Video S1). After complete wetting and subsequent drying, the OP-based samples exhibit severe warping and cracking, indicative of highly nonuniform drying stresses (Figure S3). In stark contrast, BP maintains morphological and dimensional stability throughout droplet dripping and prolonged liquid contact (Figure 3A(ii) and Video S2). The PEDOT:PSS suspension spreads uniformly across the BP surface without inducing macroscopic deformation, yielding a smooth and even film after drying (Figure S4). This behavior originates from the densified structure and strong substrate fixation of BP, which suppresses swelling-induced instabilities and enables homogeneous solvent evaporation.

The distinct wetting behaviors were quantified by contact-angle measurements, in which OP was affixed to a flat substrate to suppress water-induced macroscopic motion, whereas BP was measured directly on the substrate (Figure 3B). OP displays a high initial contact angle of 107.4°, followed by a rapid decrease to a plateau at ~40° within 4 s. By comparison, BP exhibits a substantially lower initial contact angle of 67.5° and a much faster decay within about the first second, eventually stabilizing at ~25°. The enhanced wettability of BP is attributed to the bleach-induced increase in hydroxyl and carboxyl functionalities, together with reduced surface roughness, which collectively promote rapid liquid spreading and intimate interfacial contact. As a result, PEDOT:PSS-coated BP shows a highly uniform and continuous appearance in top-view images, with no visible cracks, phase separation, or macroscopic defects (Figure S4). Side-view observations further confirm that the conductive layer closely conforms to the BP surface, forming a thin and flat coating without excessive thickness variation. Such conformality is critical for efficient charge collection and stable electrical performance. The chemical integrity of the PEDOT:PSS coating is verified by FTIR and XPS analyses (Figures 2B and S5), which reveal characteristic vibrational bands and sulfur chemical states associated with the PEDOT backbone and PSS sulfonate groups. Importantly, no signatures of oxidative degradation are observed, confirming that residual NaClO is fully removed during washing and that the bleaching process does not compromise the electronic structure of PEDOT:PSS.

A conductive adhesive tape was attached to the PEDOT:PSS layer to collect the output current signal. The PRTENG device was then completed by laminating a poly(vinyl alcohol) (PVA) overlayer (Figure 3C(i)). The assembled device exhibits good optical transparency and uniform light transmission under flashlight illumination (Figure 3C(ii)), reflecting intimate interfacial contact and defect-free integration of all functional layers. The device can be bent and curled into tight radii without cracking, delamination, or mechanical failure (Figure 3C(iii)), demonstrating excellent flexibility and mechanical compliance. Such mechanical resilience is particularly advantageous for flexible and wearable energy-harvesting applications, where repeated bending and deformation are unavoidable. Cross-sectional EDX elemental mapping reveals a continuous sulfur-rich layer localized at the interlayer, corresponding to the PEDOT:PSS coating, while carbon and oxygen are uniformly distributed throughout the substrate (Figure 3D). The interfacial architecture and bonding mechanisms are illustrated schematically in Figure 3E. The PRTENG device comprises a PVA dielectric layer, a PEDOT:PSS conductive film, and a BP substrate. At the molecular level, abundant hydrogen-bonding interactions form between hydroxyl and carboxyl groups on the BP surface and the sulfonate groups of PSS, as well as between PEDOT:PSS and the PVA overlayer. These interactions promote strong adhesion, uniform coating

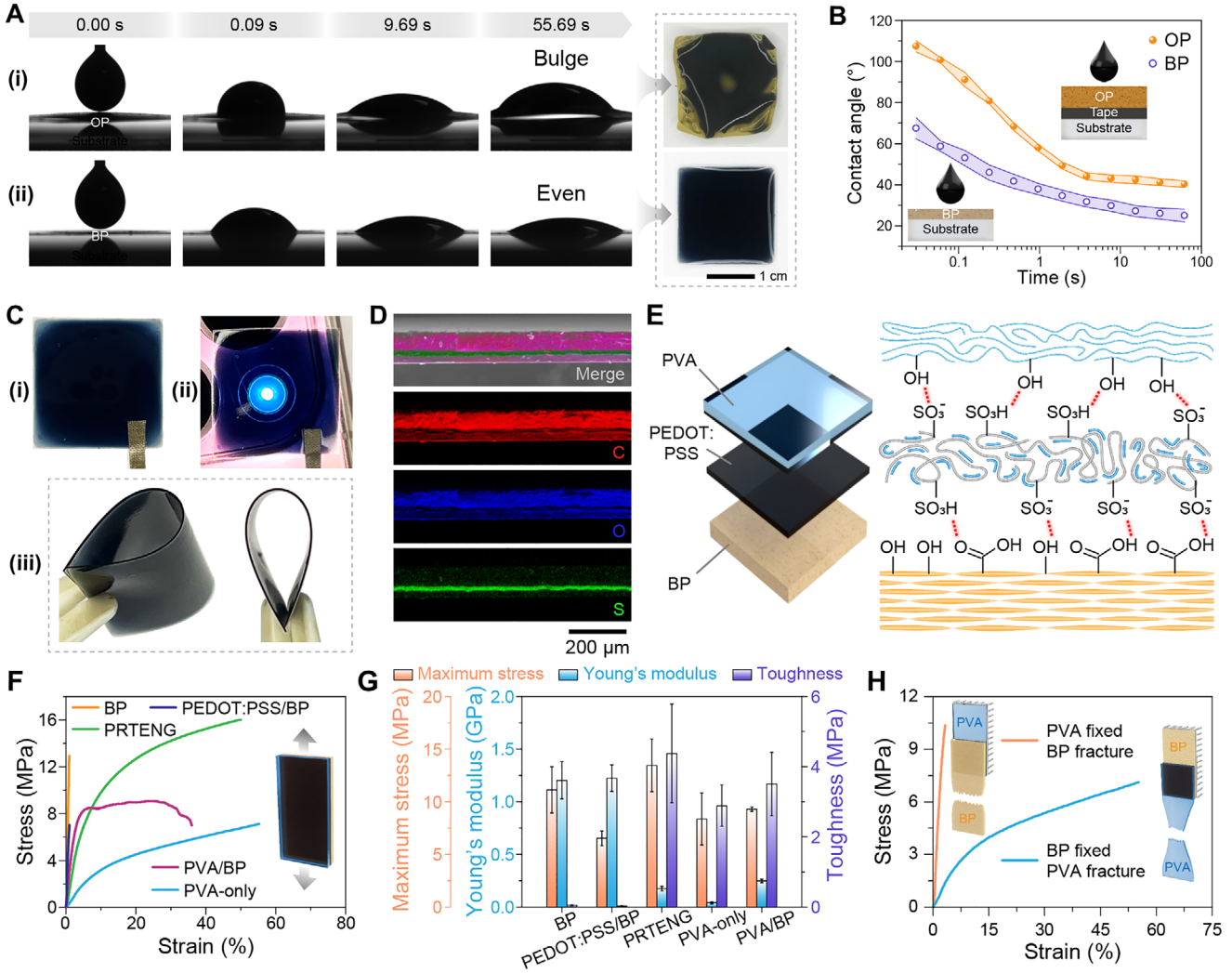

FIGURE 3 | Wetting control, device assembly, and mechanical characterization of the PRTENG. (A) Time-lapse contact angle images of a PEDOT:PSS aqueous droplet on (i) OP and (ii) BP, showing swelling-induced bulging on OP vs. stable wetting and uniform spreading on BP; right: corresponding morphology of the pollen paper after spreading of PEDOT:PSS dispersion. (B) Dynamic contact-angle evolution of a PEDOT:PSS aqueous droplet on OP and BP, demonstrating enhanced wettability (lower initial contact angle and faster decay) on BP compared with OP. All the data are represented as mean values ± s.d. from 3 samples. (C) Photographs of the assembled PRTENG device: (i) top view of PRTENG device, (ii) PRTENG under phone-flashlight illumination demonstrating optical transparency/uniformity, and (iii) bent/curling states showing mechanical flexibility. (D) Cross-sectional EDX elemental maps (C, O, S) reveal a continuous, sulfur-rich PEDOT:PSS interlayer uniformly sandwiched between the BP substrate and the PVA overlayer. (E) Schematic of the PRTENG architecture (PVA/PEDOT:PSS/BP) and proposed hydrogen-bonding interactions across the interfaces. (F) Representative tensile stress–strain curves of BP, PEDOT:PSS/BP, PVA/BP, PVA-only and the assembled PRTENG, highlighting the enhanced strength and ductility after multilayer integration. (G) Statistical analysis of maximum stress, Young's modulus, and toughness for BP, PEDOT:PSS/BP, PVA/BP, PVA-only and PRTENG. All the data are represented as mean values ± s.d. from 4 samples. (H) Tensile delamination tests with asymmetric fixation: failure occurs within BP when PVA is fixed and within PVA when BP is fixed, indicating interfacial adhesion exceeding the cohesive strength of each layer.

formation, and mechanical robustness, while also facilitating efficient charge transfer across the interfaces.

The mechanical properties of the multilayer architecture were systematically evaluated by comparing BP, PEDOT:PSS/BP, PVA-only, PVA/BP, and the fully assembled PRTENG (Figure 3F). BP and PEDOT:PSS/BP exhibit limited elongation and negligible toughness, whereas PVA-only displays pronounced ductility and considerable energy-absorption capability, confirming the intrinsic toughening contribution of PVA. Compared with PVA-only, PVA/BP exhibits increased maximum stress, Young's modulus, and toughness, indicating additional reinforcement through interfacial load transfer between PVA and BP. The fully assembled PRTENG achieves the highest maximum stress and toughness among the tested samples, including a 21% increase in maximum stress and an 82-fold enhancement in toughness relative to BP (Figure 3G). These results demonstrate that the mechanical enhancement arises from the synergistic effects of the intrinsic ductility of PVA, efficient interfacial load transfer, and hydrogen bond-mediated reinforcement within the multilayer architecture. Interlayer adhesion of the PRTENG was further assessed by tensile delamination tests with asymmetric fixation (Figure 3H).

When the PVA layer was fixed, a fracture occurred within the BP; conversely, fixing the BP shifted failure to the PVA. This switch in failure location indicates that the BP/PEDOT:PSS/PVA interfacial adhesion surpasses the intrinsic tensile strength of the constituent layers. Together, these results underscore the mechanical robustness, structural coherence, and process reliability of the PRTENG architecture enabled by bleaching-induced wetting control and interfacial reinforcement.

2.3 | Working Mechanism and Performance Optimization of the PRTENG

The working mechanism of the PRTENG is illustrated in Figure 4A. The PRTENG operates in a typical single-electrode mode, in which alternating current (AC) electrical outputs are generated through contact and separation with external objects. Here, we assume the external object is a PTFE film, which carries negative charges. Initially, a substantial amount of positive electrostatic charge accumulates on the surface of the PVA layer, as PVA is a triboelectric material with a strong tendency to gain positive charges [51]. To maintain electrostatic balance, an equal amount of negative charge is induced in the underlying PEDOT:PSS electrode (Figure 4A(i)). As the PTFE film approaches the PRTENG, its negative charges begin to screen the positive charges on the PVA surface. To maintain electrostatic equilibrium, the induced negative charges in the PEDOT electrode flow to the ground (Figure 4A(ii)). Upon full contact between the PTFE film and the PRTENG, a new electrostatic equilibrium is established, and no current flows in the external circuit (Figure 4A(iii)). When the PTFE film separates from the PRTENG, the electrostatic imbalance causes electrons to flow back into the electrode, generating a reverse current in the external circuit (Figure 4A(iv)).

According to the operation mechanism of the PRTENG, it is important to note that its electrical output is closely related to the amount of charge transferred within the circuit. Based on this principle, the performance of the PRTENG was systematically optimized and evaluated with respect to several key parameters, including the conductivity of the PEDOT:PSS electrode, the thickness of the PVA insulating layer, and the overall device size. By adjusting the volume of the PEDOT solution, the electrode thickness, and consequently its conductivity, can be dynamically tuned. As shown in Figure 4B, enhancing the conductivity of the PEDOT:PSS electrode leads to improved output performance of the PRTENG. When a small amount of PEDOT:PSS solution is used (e.g., 0.66 g/m^2), the resulting layer is too thin to form a uniform and continuous film. This significantly hinders charge transport within the circuit and results in a relatively low electrical output. As the volume of PEDOT:PSS solution increases, both the conductivity of the electrode and the output performance of the PRTENG improve. However, this enhancement reaches a plateau at 5.29 g/m^2, beyond which no further output gain is observed. At this saturation point, the maximum output voltage reaches 172 V. Regarding the thickness of the PVA insulating layer, increasing it from 32 to 192 μm initially enhances the output of the PRTENG, but further increases lead to a decline in performance with a maximum of 182 V, as shown in Figure 4C. In general, a thinner insulating layer is favorable for inducing a larger amount of charge in the electrode [52]. However, this comes at the cost of a reduced dielectric breakdown voltage, following the relation $V_{BD} = E_{BD} \times d$, where V_{BD} is the breakdown voltage, E_{BD} is the dielectric breakdown strength, and d is the thickness of the dielectric layer. If the PVA layer is too thin, localized electrical breakdown may occur during operation, which reduces electrical output. We assume that the surface charge density remains stable under natural environmental conditions. Therefore, increasing the overall size of the device will proportionally increase the total amount of transferred charges, resulting in a higher output from the PRTENG. This trend is consistent with the results shown in Figure 4D. The optimal transferred charges and short-circuit current of a 3 × 3 cm^2 device was illustrated in the Figure S10A,B.

To evaluate the maximum output performance of the PRTENG, we measured the power density as a function of external load resistance, using a device with dimensions of 3 × 3 cm^2. As shown in Figure 4E, the peak power density reached 5.07 W m^{-2} at an external load resistance of 3 × 10^6 Ω, which also corresponds to the internal impedance of the PRTENG. The output energy per cycle also could be calculated to 24.97 μJ based on the voltage-time waveform (Figure S10C and Note S1). For triboelectric-based energy harvesters, an ideal scenario involves achieving both high power density and low internal impedance, which together contribute to higher energy conversion efficiency when powering electronic devices. Based on this, we compared the power density and internal impedance of the PRTENG with those of other recyclable TENGs, as shown in Figure 4F and Table S1 [26, 43, 53–63]. The PRTENG not only exhibits a higher power density but also demonstrates a relatively lower internal impedance. This favorable performance may be attributed to the partial re-dissolution of PEDOT into the PVA layer during fabrication, which could be confirmed by the EDS results in Figure S6. Although the amount of re-dissolved PEDOT is minimal and insufficient to render the PVA layer conductive, it increases the dielectric constant of the PVA insulating layer. Actually, the single-electrode mode PRTENG can be modeled as a series of parallel-plate capacitors [64]. According to this model, an increase in the dielectric constant leads to a reduction in overall device impedance. To verify this hypothesis, we constructed three parallel-plate capacitors with different dielectric configurations: metal electrode/PTFE/metal electrode (as PTFE is a widely used material in TENGs), metal electrode/PVA/metal electrode, and metal electrode/PVA/PEDOT:PSS electrode. In each case, the dielectric layer was cast directly onto the electrode. As shown in Figure S7, the capacitor composed of a metal electrode/PVA/PEDOT:PSS electrode exhibited the highest capacitance, confirming that the PVA layer in contact with the PEDOT:PSS electrode possesses the largest dielectric constant. To further substantiate the proposed hypothesis, we quantitatively characterized the dielectric constant, dielectric loss, and leakage current density of pristine PVA and PVA/PEDOT:PSS films (Figure S11). The PVA/PEDOT:PSS sample was prepared following the same procedure used for PRTENG fabrication, thereby reproducing the interpenetrated interface present in the device. Compared with pristine PVA, the PVA/PEDOT:PSS film exhibited a higher dielectric constant and consequently a higher capacitance, which reduces the capacitive component of the internal impedance. Meanwhile, the comparable dielectric loss and low leakage current densities of the two films demonstrate that the enhanced dielectric response is not accompanied by appreciable additional dielectric dissipation or the formation of

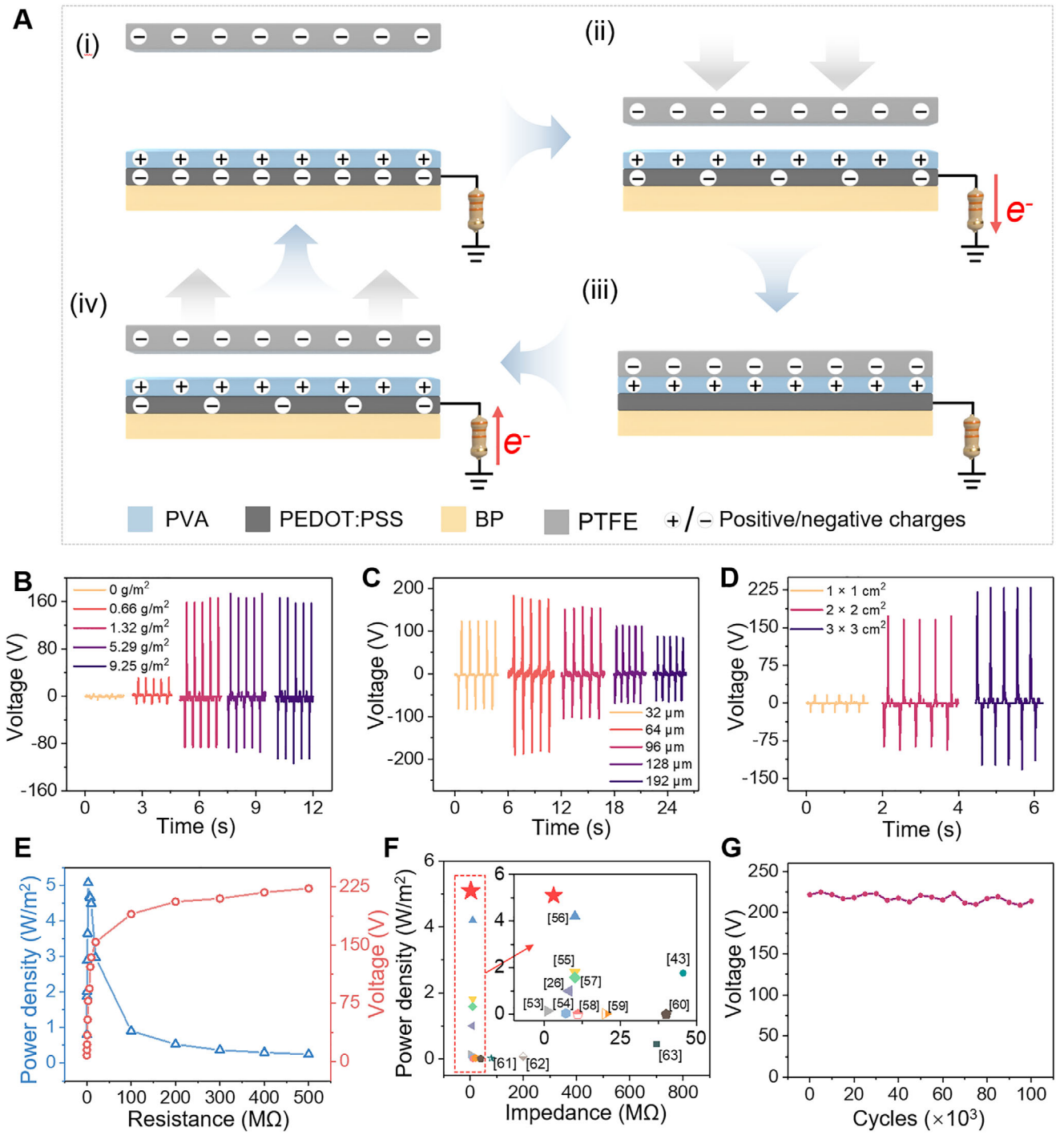

FIGURE 4 | Output characterization, parameter optimization, and durability of the PRTENG. (A) Working mechanism of the PRTENG operating in single-electrode mode. (i) Initial electrostatic equilibrium with positive tribocharges on the PVA surface and induced negative charges in the PEDOT:PSS electrode; (ii) approach of a negatively charged external object (PTFE film) screens the surface charges and drives electrons from the electrode to ground; (iii) full contact establishes a new equilibrium with no net current; (iv) separation restores electrostatic imbalance and causes electrons to flow back, generating a reverse current. (B) Dependence of the PRTENG voltage output on the PEDOT:PSS coating amount during fabrication, reflecting the effect of electrode thickness/continuity (and thus charge transport capability) on device performance. (C) Voltage output as a function of PVA dielectric-layer thickness, showing an optimum thickness that balances charge induction and dielectric breakdown robustness. (D) Scaling behavior of voltage output with overall device size (effective area), consistent with increased total transferred charge under otherwise identical operation conditions. (E) Load-matching characteristics of a 3×3 cm^2 PRTENG: voltage output and areal power density as a function of external load resistance, with the peak power density occurring near the matched resistance (corresponding to the internal impedance of the device). (F) Benchmarking of the PRTENG against reported recyclable TENGs in terms of power density and internal impedance, highlighting the favorable combination of higher power density and relatively lower impedance. (G) Cycling stability of the PRTENG over 100 000 contact–separation cycles, demonstrating robust electrical output and mechanical durability.

conductive leakage pathways. Finally, we assessed the durability of the PRTENG through cyclic testing. As illustrated in Figure 4G, the output performance of the PRTENG remained stable after 100 000 contact-separation cycles with an output retention of approximately 97%, demonstrating excellent mechanical and electrical robustness, and the durability of the PRTENG is comparable to that of previously reported contact–separation-mode and wearable TENGs (Table S2).

2.4 | Self-Powered Energy Harvesting and Wearable Applications of the PRTENG

Given the optimal performance and great durability, the PRTENG holds significant potential for practical applications, particularly as a portable energy harvester for powering wearable electronics and enabling self-powered wearable IoT systems. However, since the PRTENG generates an alternating current (AC) output, it cannot directly serve as a usable power source for most electronic devices. To address this, a self-powered system was developed to regulate the output and store the harvested energy in capacitors, as illustrated in Figure 5A. The AC output could be converted into direct current (DC) via a rectification circuit within the system (Figure 5B). The rectified average output power was determined by integrating the voltage–time waveform recorded across the optimal 3 MΩ load over eight consecutive cycles, yielding a value of 29.43 μW (Figure S10D and Note S1). Then, to evaluate the energy storage performance of the PRTENG, a series of capacitors with different capacitances were tested. As shown in Figure 5C, capacitors of 2.2, 4.7, 10, and 22 μF were charged to 3 V within 5.8, 12.1, 36.5, and 72.4 s, respectively. These results demonstrate PRTENG's capability to effectively power energy storage units. To further validate the practical applicability of the self-powered system, we used it to operate commercial electronic devices. A linear motor was employed to simulate periodic contact-separation at 1 Hz, mimicking the rhythm of human walking. Under this setup, a 3×3 cm^2 PRTENG charged a 10 μF capacitor to 4.1 V within 13 s. The stored energy was sufficient to continuously power a clock, as long as the mechanical input was maintained (Figure 5D and Video S3). Similarly, a commercial calculator was also successfully powered by the system. In this case, the PRTENG charged a 22 μF capacitor to 4.7 V within 32 s, enabling the calculator to function continuously and perform computations (Figure 5E and Video S4).

To further demonstrate the feasibility of the PRTENG as a wearable power source, we integrated the device into a pair of shoes (Figures 5F and S8), and the mode of motion will thus significantly influence the performance of this self-powering system. As illustrated in Figure 5G, the PRTENG-based self-powered system generated a ~1 Hz DC output during walking and a ~3 Hz DC output during running movements, indicating that more vigorous motion, such as running, results in a faster energy generation rate. For instance, a 10 μF capacitor could be charged to 3 V within 50 s while walking, but only requires 16 s during running, which is approximately three times faster. However, benefiting from the high power density and low internal impedance of the PRTENG, the self-powering system can also efficiently operate under slower movements. As demonstrated in Figure 5I and Video S5, just four walking steps were sufficient to charge a 1 μF capacitor to 2.5 V, which was enough to power an electronic watch and enable its proper operation. In addition, as a wearable device, the stability of the PRTENG's performance under deformation is crucial. Therefore, we measured its voltage output after undergoing bending deformation, as shown in Figure S9. Even after 10 000 bending cycles, the PRTENG maintained stable performance, demonstrating excellent durability. To further evaluate the practical applicability of the PRTENG, we have further added sliding-friction durability and humidity-dependent stability tests, as shown in Figure S12. The device maintained a stable electrical output over 100 000 sliding-friction cycles against cotton fabric, demonstrating good durability under repeated lateral mechanical contact (Figure S12A). Moreover, stable cyclic outputs were obtained at relative humidity levels ranging from 60% to 90%, confirming reliable operation under humid conditions relevant to footwear applications (Figure S12B). Interestingly, the output gradually increased with increasing relative humidity, which may be associated with moisture-induced changes in the surface polarity, mechanical compliance, and effective contact area of the hydroxyl-rich PVA layer [65, 66]. These results demonstrate that the PRTENG possesses comparable stability under both repeated sliding and high-humidity operating conditions.

2.5 | Water-Responsive Disassembly Enables Closed-Loop Recycling and Rapid Biodegradation of PRTENGs

The PRTENG demonstrates outstanding recyclability enabled by the water-responsive nature of its constituent layers. As shown in Figure 6A, immersing the device in water initiates a gradual delamination of the PEDOT:PSS electrode from the BP substrate. Upon soaking, the PEDOT:PSS layer swells and rapidly loses adhesion (Figure 6A(i–iii)), followed by complete detachment and dispersion of the conductive polymer into the surrounding aqueous medium (Figure 6A(iv)). Concurrently, the adhesive strength of the electrode tape is markedly reduced, allowing it to be removed cleanly from the device after several gentle rinsing steps (Figure 6A(v–vii)). After the conductive coating and electrode tape are fully separated, a nearly pristine BP substrate is recovered, as evidenced by the transparent region highlighted in Figure 6A(viii). This simple, water-assisted disassembly route not only enables facile separation of functional components for potential reuse or recycling, but also underscores the intrinsically green and solvent-free recyclability of the PRTENG architecture, aligning well with the sustainability requirements for next-generation transient and eco-friendly electronic systems.

Beyond facile water-assisted disassembly, the PRTENG enables closed-loop recovery of its functional components. After soaking and rinsing, the detached PEDOT:PSS readily redisperses in the aqueous phase and can be efficiently recovered by centrifugation (Figure 6B), providing a practical route to reuse the conductive material without introducing organic solvents or harsh reagents. In parallel, the BP maintains its macroscopic integrity during the soaking process; upon drying, the substrate restores a uniform morphology suitable for reutilization, supporting repeated device fabrication cycles. Leveraging this component-level separability, the recovered paper and electrode materials are reassembled into a new PRTENG (Figure 6C). Importantly, recycling does not compromise device function: the output voltage remains essentially unchanged over five consecutive recycle–rebuild cycles

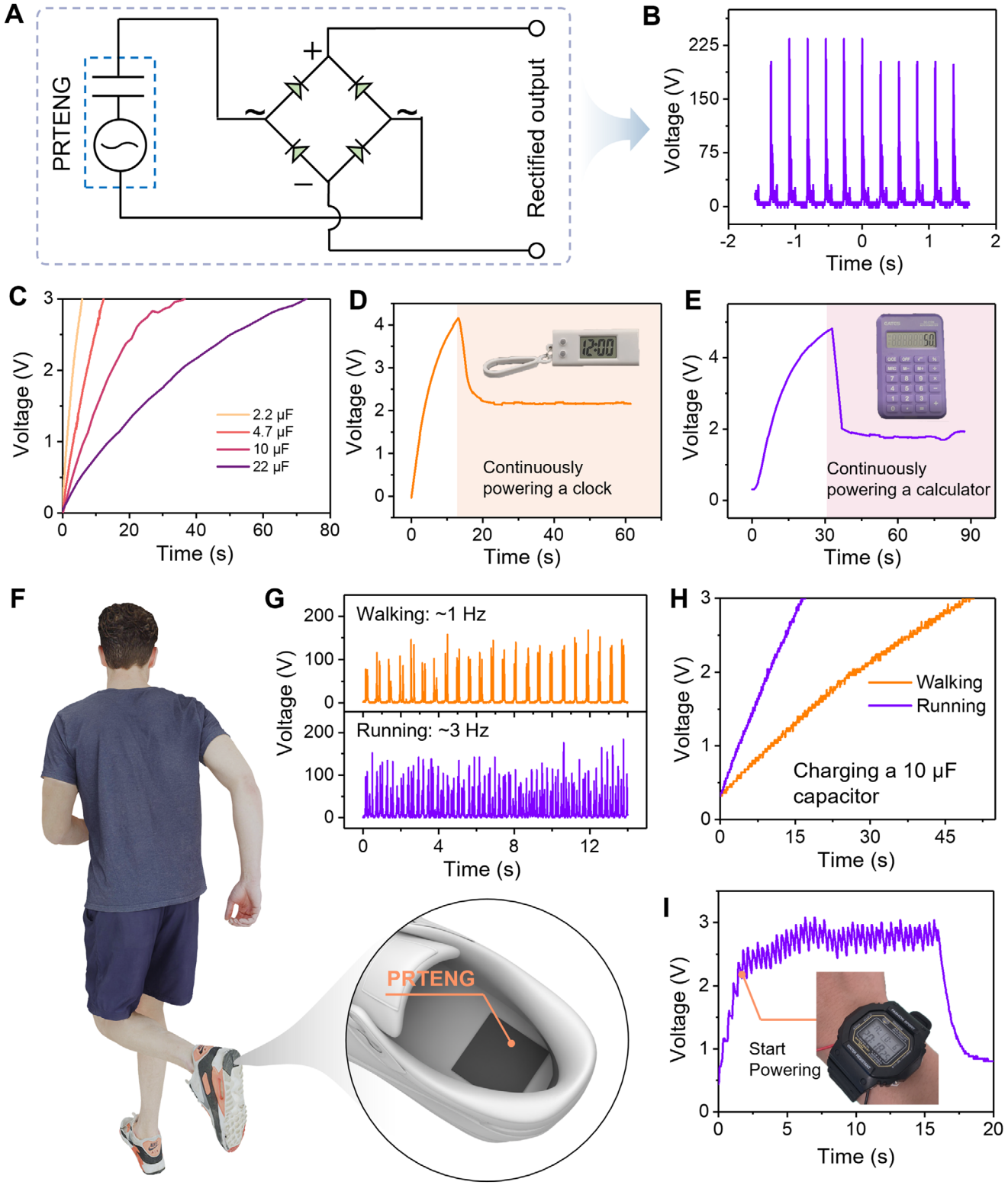

FIGURE 5 | PRTENG-based self-powered power management system and demonstrations in portable/wearable electronics. (A) Schematic/equivalent circuit of the self-powered system integrating the PRTENG, a full-wave rectifier, and a storage capacitor, enabling conversion of the alternating-current output into a regulated direct-current supply for electronic loads. (B) Representative rectified DC output waveform of the PRTENG after the rectification circuit, confirming successful AC-to-DC conversion. (C) Capacitor charging characteristics of the rectified output using capacitors with different capacitances, showing the voltage evolution as a function of charging time and demonstrating effective energy storage capability. (D) Demonstration of powering a commercial clock: a 3×3 cm^2 PRTENG charges a 10 μF capacitor to the operation voltage, after which the stored energy drives the clock continuously under periodic mechanical excitation. (E) Demonstration of powering a commercial calculator: the PRTENG charges a 22 μF capacitor to an appropriate voltage to enable stable calculator operation and continuous computations. (F) Photograph/schematic of a wearable configuration where the PRTENG is integrated into a pair of shoes to harvest biomechanical energy during human motion, forming a wearable self-

(Figure 6D), with values clustered near ~210 V and showing only minor variation. This stable electrical response indicates minimal interfacial or electrode degradation during aqueous processing and highlights the robustness of the PEDOT:PSS/pollen-paper architecture. Collectively, a scalable strategy for recyclable, high-performance triboelectric systems was established, where both the active electrode and the biobased substrate can be recovered and re-integrated with negligible loss of output.

In addition to recyclability, the PRTENG platform offers a clear end-of-life advantage through the rapid environmental degradation of its biobased substrate. After recovering the electrode tape and PEDOT:PSS coating, the BP was directly exposed to a natural soil environment to evaluate biodegradability (Figure S13). As shown in Figure 6E, the substrate exhibits pronounced physical disintegration within the first few days, followed by progressive fragmentation and mass loss; notably, the sample completely disappears within 12 days, indicating fast biodegradation under ambient conditions. This behavior contrasts sharply with conventional flexible electronic substrates based on commodity polymers–-such as polyethylene (PE), polyethylene terephthalate (PET), polypropylene (PP), and polydimethylsiloxane (PDMS) films–-which typically persist in the environment and accumulate as long-lived waste. To quantitatively evaluate the degradation behavior of the BP substrate, its residual mass was monitored during natural outdoor exposure. As shown in Figure S14, the residual mass decreased progressively with exposure time and approached zero by Day 11, consistent with the gradual fragmentation and disappearance observed in the photographic images. Collectively, these results establish a component-specific circular end-of-life strategy for the PRTENG, integrating the recovery and reuse of functional components with the natural degradation of the biobased BP substrate. This dual-pathway design provides a sustainable framework for next-generation transient and recyclable electronics.

3 | Conclusion

In summary, this study established a sustainable framework for triboelectric energy harvesting via a flexible, recyclable, and eco-friendly TENG, based on natural plant pollen. The bleaching treatment effectively alters the chemical composition and surface properties of the pollen paper, resulting in a highly conformable substrate with enhanced interfacial affinity. The synergistic interactions between BP, PEDOT:PSS, and PVA, through strong interlayer bonds, achieved a mechanically robust PRTENG with a 21% increase in maximum stress and an 82-fold increase in toughness relative to a pristine BP. The optimized interfacial architecture and material design enabled PRTENG to exhibit a peak power density of 5.07 W m^{-2} and demonstrate stable electrical output after over 30 000 contact-separation cycles. The high-power density and low internal impedance enable efficient energy harvesting and storage, sufficient to charge capacitors and power portable electronic devices. The integration of PRTENG into footwear enables the effective conversion of human motions into electrical energy, underscoring its potential as a wearable power source for self-powered electronics. Critically, the carefully engineered device architecture enables a facile water-assisted disassembly, facilitating the successful separation and recovery of the PEDOT:PSS electrode and pollen substrate. The recovered components were reassembled with minimal loss in performance. Moreover, the recovered BP exhibits biodegradation in natural soil, providing a sustainable end-of-life pathway and addressing the pressing issues faced by synthetic polymeric TENG.

Besides, this study advances the concepts of cross-economy by transforming low-value pollen into a high-value multifunctional substrate, charting a potential pathway toward the utilization of biomass-derived functional platforms for sustainable energy harvesting technologies. Future work could focus on enhancing electrical properties by employing surface micro-structuring, composition optimization, and advanced device integration strategies. In parallel, extending the framework to other biowaste and scalable manufacturing techniques could accelerate the development of sustainable, biomass-derived, and biodegradable electronic systems. Overall, these advances are envisioned to pave the way toward fully sustainable deployment in wearable electronics, decentralized sensing networks, and next-generation sustainable IoT infrastructures.

4 | Experimental Section

4.1 | Materials and Reagents

Defatted pollen powder derived from natural Camellia grains was provided by Yuensun Biological Technology Co., Ltd. Acetic acid (ACS reagent grade), acetone (AR grade), poly(3,4-ethylenedioxythiophene):poly(styrene sulfonate) (PEDOT:PSS, high-conductivity grade, 1.1% in H_2O), poly(vinyl alcohol) (PVA), absolute ethanol, and sodium hypochlorite solution (NaClO, available chlorine 4–4.99%, reagent grade) were purchased from Sigma–Aldrich. Potassium hydroxide was sourced from VWR Chemicals. Diethyl ether (AR grade) was obtained from Schedelco Pte. Ltd. All chemicals were used without further purification unless otherwise stated. Deionized (DI) water was obtained from a Milli-Q M water purification system (Merck). Nylon mesh was purchased from ELKO Filtering Co. LLC. Polyimide (PI) tape (Kaizhen; layer thickness 0.175 mm) was obtained from Shenzhen Changdasheng Electronics Co., Ltd.

4.2 | Defatting of Pollen Grains

Natural Camellia pollen grains (500 g) were dispersed in DI water (1 L) at 50°C and stirred at 1000 RPM for 2 h (Eurostar 20

powered system. (G) Rectified DC output signals generated during walking (~1 Hz) and running (~3 Hz), indicating that more vigorous motion increases the effective energy generation rate. (H) Comparison of charging profiles of a 10 μF capacitor under walking vs. running, showing faster charging during running due to higher excitation frequency. (I) Practical wearable demonstration: only a few walking steps charge a capacitor to a sufficient voltage to power an electronic watch, validating the feasibility of the wearable self-powered system for low-power portable electronics.

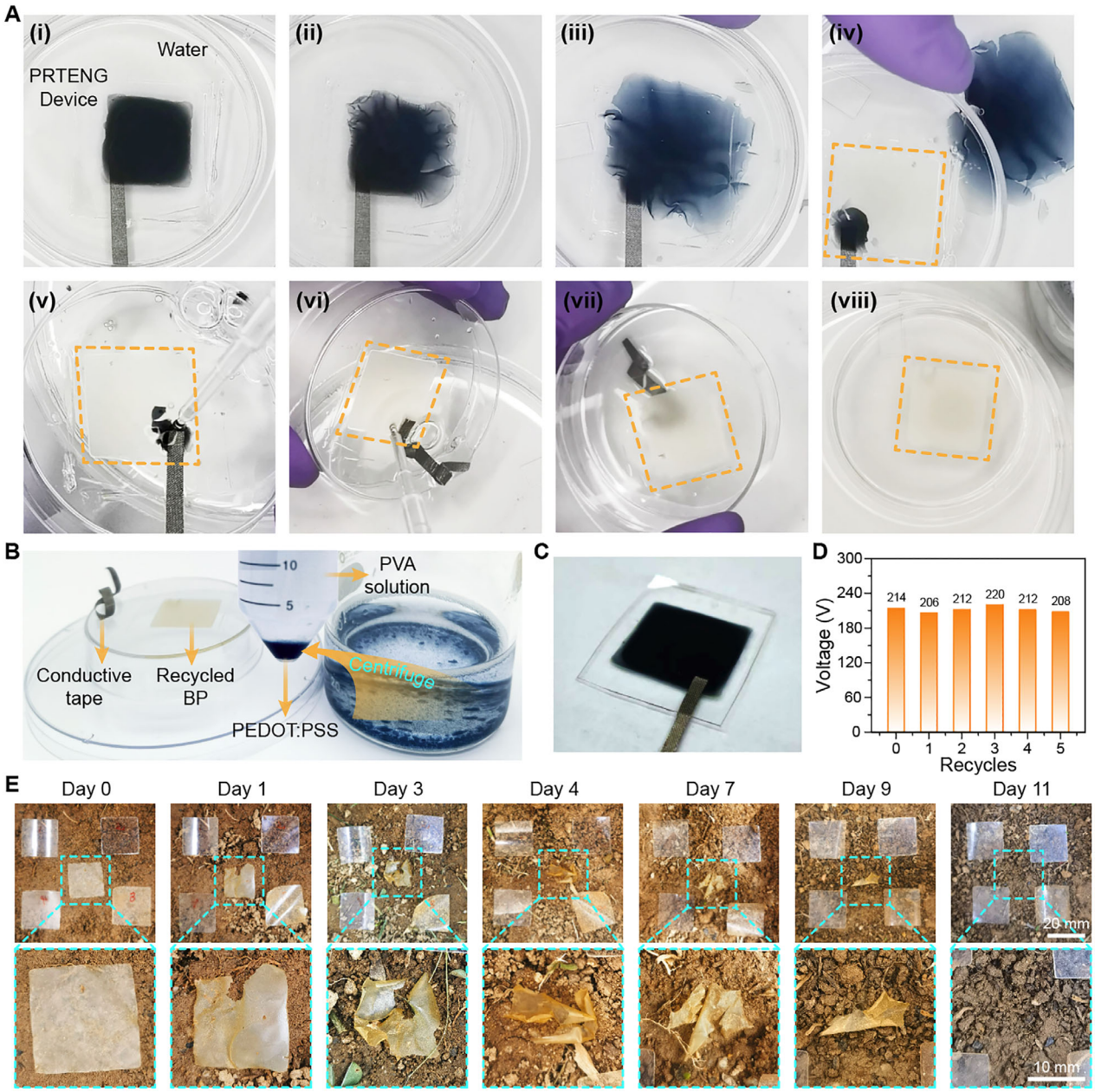

FIGURE 6 | Recyclability and biodegradability of the PRTENG. (A) Stepwise disassembly and removal of the conductive layer from a water-immersed device, enabling separation of device components (iv–viii, dashed boxes indicate the recovered BP region). (B) Collection of the separated constituents, including conductive tape, recycled BP substrate, recovered PEDOT:PSS, and PVA solution for reuse. (C) Photograph of a reconstructed PRTENG fabricated from the recovered components. (D) Electrical output voltage of the reconstructed devices over multiple recycling cycles, demonstrating stable performance. (E) Time-lapse photographs showing progressive biodegradation of the BP substrate on natural soil over 12 days (top: whole samples; bottom: magnified views of dashed regions). Starting from the upper left corner and proceeding clockwise, the control samples are polyethylene (PE), polyethylene terephthalate (PET), polypropylene (PP), and polydimethylsiloxane (PDMS).

digital, IKA). The suspension was filtered through a nylon mesh (200 μm pore size) and vacuum-filtered to remove excess water. The resulting slurry was redispersed in acetone (1 L) at room temperature for 3 h under vigorous stirring (1000 RPM), followed by vacuum filtration. The pollen was washed with fresh acetone until the filtrate was clear and air-dried for 12 h. The dried pollen (~150 g) was further defatted by two extraction cycles in diethyl ether (1 L each; 1000 RPM, room temperature, 2 h per cycle), followed by vacuum filtration. A final extraction was carried out in diethyl ether (1 L) for 12 h under identical conditions. The defatted pollen powder was collected by vacuum filtration and air-dried overnight before use.

4.3 | Preparation of Pollen Paper

Defatted pollen (30 g) was dispersed in 10% (w/v) KOH solution (300 mL) in a Teflon round-bottom flask and refluxed at 80°C for 2 h under stirring (800 RPM). The resulting suspension was filtered through a custom-built filtration device fitted with a nylon

mesh (35 μm pore size), and the residue was washed with fresh 10% KOH until the filtrate became clear. The sample was then resuspended in fresh 10% KOH solution (300 mL), divided equally into eight centrifuge tubes (40 mL per tube), vortexed at high speed for 2 min, and incubated at 80°C for 40 h. After incubation, the suspension was filtered again through the same 35 μm nylon mesh and thoroughly rinsed with DI water until a neutral pH was reached. Excess water was removed by centrifugation (3000 RPM, 5 min) to obtain a pollen-derived microgel, which was cast into a Petri dish and air-dried under ambient conditions to yield the pollen paper.

4.4 | PRTENG Fabrication

A bleach solution (pH 9.0) was prepared by the dropwise addition of acetic acid to an aqueous NaClO solution under continuous stirring in a fume hood. The freshly prepared solution was immediately used to treat the pollen paper, which was agitated at 80 rpm for 30 min on an orbital shaker (Heidolph Unimax 1010). After bleaching, the pollen paper was rinsed three times with deionized (DI) water, followed by three washes with ethanol. Between the final two ethanol washes, the process was temporarily paused until the color of the pollen paper stabilized. Following the washing steps, the bleached pollen paper was uniformly spread on a flat and smooth substrate (Petri dish or glass slide) and air-dried overnight at ambient conditions. A PEDOT:PSS suspension was then evenly applied to the dried pollen paper with recorded volume and air-dried completely. A 5 mm-wide conductive tape (Shenzhen Kangqian Jintai Technology Co., Ltd.) was subsequently affixed securely to one corner of the PEDOT:PSS-coated paper. 20% (w/v) PVA aqueous solution was gently poured onto the paper and dried overnight. To control the thickness and ensure the uniformity of the PVA layer, a square reservoir was constructed to enclose the pollen paper (Figure S15) before pouring PVA. Each wall of the reservoir was compactly stacked with multiple layers of PI tapes. To minimize PVA film thickness nonuniformity arising from liquid bridge effects at the reservoir walls, the distance between the wall and the paper edge was maintained at greater than 1 cm. The device was then peeled from the substrate, and fabrication was finally completed after trimming the excess peripheral PVA film.

4.5 | Electrical Tests of PRTENGs

The electrical output of the contact–separation generator was recorded using an oscilloscope (TBS2104B, Tektronix). A stepper motor (LM1225QI, DAZEJIDIAN Ltd.) was employed to precisely control the periodic contact–separation motion. During testing, the counter object was driven in a linear reciprocating manner with a maximum separation distance of 10 mm, and the moving speed was set to 100 mm s^{-1}. Unless otherwise specified, all measurements were conducted under ambient conditions.

4.6 | Imaging and Characterization

The morphological features of the materials were photographed using an iPhone 12 and further characterized by field-emission scanning electron microscopy (FE-SEM, 7800F). Chemical composition was analyzed by Fourier transform infrared spectroscopy (FTIR, PerkinElmer, Frontier) and x-ray photoelectron spectroscopy (XPS, 225 W Al Kα radiation, Kratos AXIS Supra). Elemental composition and spatial distribution were examined using SEM-associated energy-dispersive x-ray (EDX) spectroscopy. Surface topographies were obtained by atomic force microscopy (AFM; Park Systems, NX10). The modulus of the samples was measured after ethanol washing using a rotational rheometer (Anton Paar, MCR 702e) with steel parallel-plate geometry. A humidity chamber was employed to cover the experimental setup, preventing any rapid evaporation during testing. A preliminary equilibration was performed for 3 min before testing. The test moving profile was set to "Gel auto-F | 1 N". The modulus was determined by a strain amplitude sweep at a frequency of 1 rad/s over a strain range of 0.1%–10%. The wettability of the materials was evaluated using an optical contact angle goniometer (Data Physics, OCA 15 Pro) via the sessile drop method. Mechanical properties were assessed using a dynamic mechanical analyzer (DMA Q800, TA Instruments). Tensile tests were performed at room temperature under a constant loading rate of 2 N/min until failure.

4.7 | Recyclability Test

The used device was first immersed in warm DI water (~45°C [67]) for 30 min to facilitate dissolution of the PVA film and detachment of the conductive film. Subsequently, the device was rinsed with warm DI water until no residue remained on the pollen paper surface. After washing 3 times with ethanol, the paper was fully air-dried. The washing solution containing the detached PEDOT:PSS was collected into a 50 mL centrifuge tube and centrifuged at 3000 rpm for 10 min. The PEDOT:PSS was then recovered after removal of the supernatant, which can be redeposited onto the recycled paper substrate to form the conductive layer again. The recycled device was finally completed after attaching the conductive tape and reapplying the PVA as mentioned above.

4.8 | Biodegradability Test

The biodegradability of the detached pollen substrate was evaluated under natural environmental conditions and benchmarked against common commercial polymeric materials, including PE, PET, PP, and PDMS. All materials were cut into 2 × 2 cm^2 specimens and placed at an open natural grassland site in Singapore. To minimize wind-induced displacement, the specimens were enclosed within a fixed foam box with top and bottom removed (Figure S13). Morphological changes of different samples were monitored and documented by periodic photographic recording at intervals of 1–3 days throughout the exposure period. Meanwhile, the specimens were retrieved, cleaned, dried to a constant mass, and weighed at predetermined time points to obtain the residual mass curve as a function of exposure time.

Author Contributions

Zihao Guo: formal analysis, investigation, software, data curation, visualization, writing – review and editing, conceptualization, writing – original draft, methodology, validation. **Jun Hao Mo**: investigation,

writing – original draft, validation. **Chenchen Zhou**: conceptualization, methodology, software, data curation, investigation, validation, writing – review and editing, writing – original draft, visualization, formal analysis. **Daru Seto Bagus Anugrah**: methodology, validation, formal analysis. **Hailu Wang**: methodology, investigation. **Dan Sun**: data curation, investigation, formal analysis, writing – original draft, writing – review and editing, methodology, validation. **Munho Kim**: supervision, validation, data curation, resources. **Nam–Joon Cho**: writing – review and editing, funding acquisition, conceptualization, project administration, supervision, resources. **Licong Yang**: methodology, validation, formal analysis.

Acknowledgements

The authors would like to thank all the TSSM group members for their various support. This study was supported by the Ministry of Education in Singapore under the MOE AcRF Tier 3 grant (Grant No. MOE-MOET32022-0002), the startup funds of Shanghai Jiao Tong University, as well as the Korea Health Technology R&D Project through the Korea Health Industry Development Institute (KHIDI), funded by the Ministry of Health & Welfare, Republic of Korea (Grant No. HI22C1394) and Ministry of Agriculture, Food and Rural Affairs (Grant No. RS-2024-00403067).

Funding

Singapore Ministry of Education, MOE AcRF Tier 3 grant (Grant No. MOE-MOET32022-0002), Korea Health Technology R&D Project by the Ministry of Health & Welfare, Republic of Korea (Grant No. HI22C1394), and Ministry of Agriculture, Food and Rural Affairs (Grant No. RS-2024-00403067).

Conflicts of Interest

The authors declare no conflicts of interest.

Data Availability Statement

The data that support the findings of this study are available from the corresponding author upon reasonable request.

References

1. A. Al-Fuqaha, M. Guizani, M. Mohammadi, M. Aledhari, and M. Ayyash, "Internet of Things: A Survey on Enabling Technologies, Protocols, and Applications," *IEEE Communications Surveys & Tutorials* 17 (2015): 2347–2376, https://doi.org/10.1109/COMST.2015.2444095.

2. K. Zhou, S. Yang, and Z. Shao, "Energy Internet: The Business Perspective," *Applied Energy* 178 (2016): 212–222, https://doi.org/10.1016/j.apenergy.2016.06.052.

3. S. Hu, S. Chang, G. Xiao, et al., "A Stretchable Multimode Triboelectric Nanogenerator for Energy Harvesting and Self-Powered Sensing," *Advanced Materials Technologies* 7 (2022): 2100870, https://doi.org/10.1002/admt.202100870.

4. Z. L. Wang, J. Chen, and L. Lin, "Progress in Triboelectric Nanogenerators as a New Energy Technology and Self-powered Sensors," *Energy & Environmental Science* 8 (2015): 2250–2282, https://doi.org/10.1039/C5EE01532D.

5. F. R. Fan, W. Tang, and Z. L. Wang, "Flexible Nanogenerators for Energy Harvesting and Self-Powered Electronics," *Advanced Materials* 28 (2016): 4283–4305, https://doi.org/10.1002/adma.201504299.

6. X. Zhang, L. Li, E. Fan, et al., "Toward Sustainable and Systematic Recycling of Spent Rechargeable Batteries," *Chemical Society Reviews* 47 (2018): 7239–7302, https://doi.org/10.1039/C8CS00297E.

7. J. Mao, C. Ye, S. Zhang, et al., "Toward Practical Lithium-ion Battery Recycling: Adding Value, Tackling Circularity and Recycling-oriented Design," *Energy & Environmental Science* 15 (2022): 2732–2752, https://doi.org/10.1039/D2EE00162D.

8. Z. L. Wang, "Triboelectric Nanogenerators as New Energy Technology for Self-Powered Systems and as Active Mechanical and Chemical Sensors," *ACS Nano* 7 (2013): 9533–9557, https://doi.org/10.1021/nn404614z.

9. J. Chen, Y. Huang, N. Zhang, et al., "Micro-cable Structured Textile for Simultaneously Harvesting Solar and Mechanical Energy," *Nature Energy* 1 (2016): 16138, https://doi.org/10.1038/nenergy.2016.138.

10. Z. L. Wang and A. C. Wang, "On the Origin of Contact-electrification," *Materials Today* 30 (2019): 34–51, https://doi.org/10.1016/j.mattod.2019.05.016.

11. M. S. Alghamdi, J. J. Morgan, K. Walsh, et al., "Triboelectric Nanogenerator Based on Cellulose Nanocrystals and Graphene for Energy Harvesting From Piano Playing Motion," *Nano Energy* 138 (2025): 110816, https://doi.org/10.1016/j.nanoen.2025.110816.

12. L. Li, R. Wang, Y. Fu, et al., "Fabricating and Engineering Woody-Biomass Aerogels for High-Performance Triboelectric Nanogenerators for Energy Harvesting and Biomechanical Monitoring," *Advanced Functional Materials* 35 (2024): 2412324, https://doi.org/10.1002/adfm.202412324.

13. Y. Pang, X. Zhu, C. Lee, and S. Liu, "Triboelectric Nanogenerator as next-generation Self-powered Sensor for Cooperative Vehicle-infrastructure System," *Nano Energy* 97 (2022): 107219, https://doi.org/10.1016/j.nanoen.2022.107219.

14. I. Mehamud, P. Marklund, M. Björling, and Y. Shi, "Machine Condition Monitoring Enabled by Broad Range Vibration Frequency Detecting Triboelectric Nano-generator (TENG)-based Vibration Sensors," *Nano Energy* 98 (2022): 107292, https://doi.org/10.1016/j.nanoen.2022.107292.

15. O. Demircioglu, M. O. Cicek, D. Doganay, et al., "Triboelectric Nanogenerators for Blue Energy Harvesting in Simulated Wave Conditions," *Nano Energy* 107 (2023): 108157, https://doi.org/10.1016/j.nanoen.2022.108157.

16. S. Fu, W. He, H. Wu, et al., "High Output Performance and Ultra-Durable DC Output for Triboelectric Nanogenerator Inspired by Primary Cell," *Nano-Micro Letters* 14 (2022): 155, https://doi.org/10.1007/s40820-022-00898-2.

17. D. Tan, Q. Zeng, X. Wang, et al., "Anti-Overturning Fully Symmetrical Triboelectric Nanogenerator Based on an Elliptic Cylindrical Structure for all-Weather Blue Energy Harvesting," *Nano-Micro Letters* 14 (2022): 124, https://doi.org/10.1007/s40820-022-00866-w.

18. Y. Zi, L. Lin, J. Wang, et al., "Triboelectric–Pyroelectric–Piezoelectric Hybrid Cell for High-Efficiency Energy-Harvesting and Self-Powered Sensing," *Advanced Materials* 27 (2015): 2340–2347, https://doi.org/10.1002/adma.201500121.

19. Z. L. Wang, "Triboelectric Nanogenerator (TENG)--Sparking an Energy and Sensor Revolution," *Advanced Energy Materials* 10 (2020): 2000137.

20. C. Liu and A. J. Bard, "Electrostatic Electrochemistry at Insulators," *Nature Materials* 7 (2008): 505–509, https://doi.org/10.1038/nmat2160.

21. H. T. Baytekin, A. Z. Patashinski, M. Branicki, B. Baytekin, S. Soh, and B. A. Grzybowski, "The Mosaic of Surface Charge in Contact Electrification," *Science* 333 (2011): 308–312, https://doi.org/10.1126/science.1201512.

22. G. Zhu, J. Chen, T. Zhang, Q. Jing, and Z. L. Wang, "Radial-arrayed Rotary Electrification for High Performance Triboelectric Generator," *Nature Communications* 5 (2014): 3426, https://doi.org/10.1038/ncomms4426.

23. Q. Jing, Y. Xie, G. Zhu, R. P. S. Han, and Z. L. Wang, "Self-powered Thin-film Motion Vector Sensor," *Nature Communications* 6 (2015): 8031, https://doi.org/10.1038/ncomms9031.

24. B. Meng, W. Tang, Z.-H. Too, et al., "A Transparent Single-friction-surface Triboelectric Generator and Self-powered Touch Sensor," *Energy & Environmental Science* 6 (2013): 3235, https://doi.org/10.1039/c3ee42311e.

25. M. Shanbedi, H. Ardebili, and A. Karim, "Polymer-based Triboelectric Nanogenerators: Materials, Characterization, and Applications," *Progress in Polymer Science* 144 (2023): 101723, https://doi.org/10.1016/j.progpolymsci.2023.101723.

26. T. Wang, S. Li, X. Tao, et al., "Fully Biodegradable Water-soluble Triboelectric Nanogenerator for human Physiological Monitoring," *Nano Energy* 93 (2022): 106787, https://doi.org/10.1016/j.nanoen.2021.106787.

27. H. Zou, Y. Zhang, L. Guo, et al., "Quantifying the Triboelectric Series," *Nature Communications* 10 (2019): 1427.

28. M. Sahu, S. Hajra, S. Panda, et al., "Waste Textiles as the Versatile Triboelectric Energy-harvesting Platform for Self-powered Applications in Sports and Athletics," *Nano Energy* 97 (2022): 107208, https://doi.org/10.1016/j.nanoen.2022.107208.

29. K. Chen, Y. Y. Li, G. G. Yang, et al., "Fabric-Based TENG Woven With Bio-Fabricated Superhydrophobic Bacterial Cellulose Fiber for Energy Harvesting and Motion Detection," *Advanced Functional Materials* 33 (2023): 2304809.

30. J. Jiao, Q. Lu, Z. Wang, Y. Qin, and X. Cao, "Sandwich as a Triboelectric Nanogenerator," *Nano Energy* 79 (2021): 105411, https://doi.org/10.1016/j.nanoen.2020.105411.

31. H. Liu, Q. Shu, H. Xiang, H. Wu, Z. Li, and H. Zhou, "Fully Degradable Triboelectric Nanogenerator Using Graphene Composite Paper to Replace Copper Electrodes for Higher Output Performance," *Nano Energy* 108 (2023): 108223, https://doi.org/10.1016/j.nanoen.2023.108223.

32. C. Wu, A. C. Wang, W. Ding, H. Guo, and Z. L. Wang, "Triboelectric Nanogenerator: A Foundation of the Energy for the New Era," *Advanced Energy Materials* 9 (2019): 1802906, https://doi.org/10.1002/aenm.201802906.

33. X. Pu, M. Liu, X. Chen, et al., "Ultrastretchable, transparent triboelectric nanogenerator as electronic skin for biomechanical energy harvesting and tactile sensing," *Science Advances* 3 (2017): 1, https://doi.org/10.1126/sciadv.1700015.

34. L. Zhang, Y. Liao, Y.-C. Wang, et al., "Cellulose II Aerogel-Based Triboelectric Nanogenerator," *Advanced Functional Materials* 30 (2020): 2001763, https://doi.org/10.1002/adfm.202001763.

35. J. Ahn, J.-S. Kim, Y. Jeong, et al., "All-Recyclable Triboelectric Nanogenerator for Sustainable Ocean Monitoring Systems," *Advanced Energy Materials* 12 (2022): 2201341, https://doi.org/10.1002/aenm.202201341.

36. Z. Bai, Y. Xu, J. Li, et al., "An Eco-friendly Porous Nanocomposite Fabric-Based Triboelectric Nanogenerator for Efficient Energy Harvesting and Motion Sensing," *ACS Applied Materials & Interfaces* 12 (2020): 42880–42890, https://doi.org/10.1021/acsami.0c12709.

37. T. Du, Z. Chen, F. Dong, et al., "Advances in Green Triboelectric Nanogenerators," *Advanced Functional Materials* 34 (2024): 2313794, https://doi.org/10.1002/adfm.202313794.

38. L. Y. Liu, M. J. Wu, W. T. Zhao, et al., "Progress of Triboelectric Nanogenerators With Environmental Adaptivity," *Advanced Functional Materials* 34 (2024): 2308353, https://doi.org/10.1002/adfm.202308353.

39. R. Wang, S. Gao, Z. Yang, et al., "Engineered and Laser-Processed Chitosan Biopolymers for Sustainable and Biodegradable Triboelectric Power Generation," *Advanced Materials* 30 (2018): 1706267, https://doi.org/10.1002/adma.201706267.

40. X. Shi, Y. Wei, R. Yan, et al., "Leaf Surface-microstructure Inspired Fabrication of Fish Gelatin-based Triboelectric Nanogenerator," *Nano Energy* 109 (2023): 108231, https://doi.org/10.1016/j.nanoen.2023.108231.

41. H.-J. Kim, E.-C. Yim, J.-H. Kim, S.-J. Kim, J.-Y. Park, and I.-K. Oh, "Bacterial Nano-Cellulose Triboelectric Nanogenerator," *Nano Energy* 33 (2017): 130–137, https://doi.org/10.1016/j.nanoen.2017.01.035.

42. Y. Chen, Y. Jie, J. Wang, et al., "Triboelectrification on Natural Rose Petal for Harvesting Environmental Mechanical Energy," *Nano Energy* 50 (2018): 441–447, https://doi.org/10.1016/j.nanoen.2018.05.021.

43. H. Ruan, X. Chen, C. Lv, et al., "Water-durable, and Recyclable Dynamic Cross-linked Cellulose-based Triboelectric Nanogenerators for Energy Harvesting," *Cellulose* 30 (2023): 11425–11437, https://doi.org/10.1007/s10570-023-05568-z.

44. C. Zhou, J. Deng, J. H. Tay, et al., "Multifunctional Material Building Blocks From Plant Pollen," *Annual Review of Chemical and Biomolecular Engineering* 15 (2024): 1–24, https://doi.org/10.1146/annurev-chembioeng-101121-085959.

45. Z. Zhao, Y. Hwang, Y. Yang, et al., "Actuation and Locomotion Driven by Moisture in Paper Made With Natural Pollen," *Proceedings of the National Academy of Sciences* 117 (2020): 8711–8718, https://doi.org/10.1073/pnas.1922560117.

46. T.-F. Fan, S. Park, Q. Shi, et al., "Transformation of Hard Pollen Into Soft Matter," *Nature Communications* 11 (2020): 1449, https://doi.org/10.1038/s41467-020-15294-w.

47. Y. Hwang, M. K. Kim, Z. Zhao, et al., "Plant-Based Substrate Materials for Flexible Green Electronics," *Advanced Materials Technologies* 7 (2022): 2200446, https://doi.org/10.1002/admt.202200446.

48. Y. Yu, H. Li, X. Zhang, et al., "Substantially Boosting Performance of Triboelectric Nanogenerators via a Triboelectrification Enhancement Effect," *Joule* 8 (2024): 1855–1868, https://doi.org/10.1016/j.joule.2024.04.013.

49. N.-J. Cho, "Preparing for Tomorrow With Materials Today," *Materials Today* 61 (2022): 1–3, https://doi.org/10.1016/j.mattod.2022.11.006.

50. F.-S. Li, P. Phyo, J. Jacobowitz, M. Hong, and J.-K. Weng, "The Molecular Structure of Plant Sporopollenin," *Nature Plants* 5 (2019): 41–46, https://doi.org/10.1038/s41477-018-0330-7.

51. L. Shi, S. Dong, H. Xu, et al., "Enhanced Performance Triboelectric Nanogenerators Based on Solid Polymer Electrolytes With Different Concentrations of Cations," *Nano Energy* 64 (2019): 103960, https://doi.org/10.1016/j.nanoen.2019.103960.

52. S. Niu, S. Wang, L. Lin, et al., "Theoretical Study of Contact-mode Triboelectric Nanogenerators as an Effective Power Source," *Energy & Environmental Science* 6 (2013): 3576, https://doi.org/10.1039/c3ee42571a.

53. C. Yao, A. Hernandez, Y. Yu, Z. Cai, and X. Wang, "Triboelectric Nanogenerators and Power-boards From Cellulose Nanofibrils and Recycled Materials," *Nano Energy* 30 (2016): 103–108, https://doi.org/10.1016/j.nanoen.2016.09.036.

54. Y. Lu, X. Li, J. Ping, J. He, and J. Wu, "A Flexible, Recyclable, and High-Performance Pullulan-Based Triboelectric Nanogenerator (TENG)," *Advanced Materials Technologies* 5 (2020): 1900905, https://doi.org/10.1002/admt.201900905.

55. Y. Wang, Y. Zhang, P. Ren, et al., "Versatile and Recyclable Double-network PVA/Cellulose Hydrogels for Strain Sensors and Triboelectric Nanogenerators Under Harsh Conditions," *Nano Energy* 125 (2024): 109599, https://doi.org/10.1016/j.nanoen.2024.109599.

56. Y. Ra, J. H. Lee, J. Bang, et al., "Toward Commercialization of Mechanical Energy Harvester: Reusable Triboelectric Nanogenerator Based on Closed-Loop Mass Production of Recyclable Thermoplastic Fluoropolymer With Microstructures," *International Journal of Energy Research* 2023 (2023): 6919663.

57. J. Ahn, J.-S. Kim, Y. Jeong, et al., "All-Recyclable Triboelectric Nanogenerator for Sustainable Ocean Monitoring Systems," *Advanced Energy Materials* 12 (2022): 2201341, https://doi.org/10.1002/aenm.202201341.

58. W. Zhang, J. Wang, W. Zhang, et al., "Scalable Micropatterned Epoxy Vitrimer Films by Thermo-triggered Bond Exchange for Repairable and Recyclable Triboelectric Nanogenerators," *Applied Materials Today* 32 (2023): 101789, https://doi.org/10.1016/j.apmt.2023.101789.

59. L.-N. Zhou, W.-Z. Song, D.-J. Sun, et al., "Transparent, Stretchable, and Recyclable Triboelectric Nanogenerator Based on an Acid-and Alkali-resistant Hydrogel," *ACS Applied Electronic Materials* 5 (2022): 216–226, https://doi.org/10.1021/acsaelm.2c01281.

60. H. Wang, Y. Yin, Z. Su, et al., "Bio-Based and Recyclable Self-Healing Elastomer for the Application of Self-Powered Triboelectric Nanogenerator in Low-Temperature," *Advanced Functional Materials* 34 (2024): 2311649, https://doi.org/10.1002/adfm.202311649.

61. X. Shi, P. Chen, K. Han, et al., "A Strong, Biodegradable, and Recyclable all-lignocellulose Fabricated Triboelectric Nanogenerator for Self-powered Disposable Medical Monitoring," *Journal of Materials Chemistry A* 11 (2023): 11730–11739, https://doi.org/10.1039/D3TA01763J.

62. C. Dang, C. Shao, H. Liu, Y. Chen, and H. Qi, "Cellulose Melt Processing Assisted by Small Biomass Molecule to Fabricate Recyclable Ionogels for Versatile Stretchable Triboelectric Nanogenerators," *Nano Energy* 90 (2021): 106619, https://doi.org/10.1016/j.nanoen.2021.106619.

63. S. Jiang, Y. Wang, M. Tian, et al., "Readily Recyclable, Degradable, Stretchable, Highly Conductive, Anti-freezing and Anti-drying Glycero-hydrogel for Triboelectric Nanogenerator," *Chemical Engineering Journal* 504 (2025): 158881, https://doi.org/10.1016/j.cej.2024.158881.

64. S. Niu, Y. Liu, S. Wang, et al., "Theoretical Investigation and Structural Optimization of Single-Electrode Triboelectric Nanogenerators," *Advanced Functional Materials* 24 (2014): 3332–3340, https://doi.org/10.1002/adfm.201303799.

65. J. Wang, Z. Xia, H. Yao, Q. Zhang, and H. Yang, "Self-powered TENG With High Humidity Sensitivity From PVA Film Modified by LiCl and MXene," *ACS Applied Materials & Interfaces* 15 (2023): 47208–47220, https://doi.org/10.1021/acsami.3c08706.

66. D. Liu, J. Liu, M. Yang, et al., "Performance Enhanced Triboelectric Nanogenerator by Taking Advantage of Water in Humid Environments," *Nano Energy* 88 (2021): 106303, https://doi.org/10.1016/j.nanoen.2021.106303.

67. L. V. Kayser and D. J. Lipomi, "Stretchable Conductive Polymers and Composites Based on PEDOT and PEDOT:PSS," *Advanced Materials* 31 (2019): 1806133, https://doi.org/10.1002/adma.201806133.

Supporting Information

Additional supporting information can be found online in the Supporting Information section.

Supporting File 1: aenm71517-sup-0001-SuppMat.docx.

Supporting File 2: aenm71517-sup-0002-SuppMat.docx.

Supporting File 3: aenm71517-sup-0003-VideoS1.avi.

Supporting File 4: aenm71517-sup-0004-VideoS2.avi.

Supporting File 5: aenm71517-sup-0005-VideoS3.mp4.

Supporting File 6: aenm71517-sup-0006-VideoS4.mp4.

Supporting File 7: aenm71517-sup-0007-VideoS5.mp4.